Chiral order and multiferroic domain relaxation in NaFeGe_2O_6

S. Biesenkamp, D. Gorkov, W. Schmidt, K. Schmalzl, Y. Sidis, P. Becker, L. Bohatý, M. Braden

Editors' Suggestion

Chiral order and multiferroic domain relaxation in $NaFeGe_2O_6$

S. Biesenkamp [1,*] D. Gorkov [1,2] W. Schmidt [3] K. Schmalzl [3] Y. Sidis [4] P. Becker,[5] L. Bohatý,[5] and M. Braden [1,†]

[1]*II. Physikalisches Institut, Universität zu Köln, Zülpicher Straße 77, D-50937 Köln, Germany*

[2]*Heinz Maier-Leibnitz Zentrum (MLZ), Technische Universität München, Lichtenbergstr. 1, 85748 Garching, Germany*

[3]*Juelich Centre for Neutron Science JCNS, Forschungszentrum Juelich GmbH, Outstation at ILL, 38042 Grenoble, France*

[4]*UniversitéParis-Saclay, CNRS, CEA, Laboratoire Léon Brillouin, F-91191 Gif-sur-Yvette, France*

[5]*Abteilung Kristallographie, Institut für Geologie und Mineralogie, Universität zu Köln, Zülpicher Straße 49b, 50674 Köln, Germany*

(Received 17 May 2021; revised 14 October 2021; accepted 20 October 2021; published 4 November 2021)

The magnetic structure and the multiferroic relaxation dynamics of $NaFeGe_2O_6$ were studied by neutron scattering on single crystals partially utilizing polarization analysis. In addition to the previously reported transitions, the incommensurate spiral ordering of Fe^{3+} moments in the *ac* plane develops an additional component along the crystallographic *b* direction below $T \approx 5$ K, which coincides with a lock-in of the incommensurate modulation. The quasistatic control of the spin-spiral handedness, respectively of the vector chirality, by external electric fields proves the invertibility of multiferroic domains down to the lowest temperature. Time-resolved measurements of the multiferroic domain inversion in $NaFeGe_2O_6$ reveal a simple temperature and electric-field dependence of the multiferroic relaxation that is well described by a combined Arrhenius-Merz relation, as it has been observed for $TbMnO_3$. The maximum speed of domain wall motion is comparable to the spin-wave velocity deduced from an analysis of the magnon dispersion.

DOI: 10.1103/PhysRevB.104.174405

I. INTRODUCTION

The increasing power consumption due to data storage and the growing amount of information that has to be stored or buffered enforce the development of new and more effectively working memory devices [1,2]. Aside from phase-change-based devices, skyrmion racetracks, and other promising techniques [2–9], multiferroic systems are promising for designing future storage techniques [10,11].

In multiferroics at least two ferroic ordering parameters occur in the same phase and are coupled to each other [12]. Both ordering parameters can be controlled by both conjugate fields. The magnetoelectric case with ferroelectric and magnetic ordering is most prominent, as it allows for a multiferroic memory, which combines the advantages of ferroelectric (FeRAMs) and magnetic random access memories (MRAMs) [10,11,13]. In so-called type-II multiferroics the ferroelectric polarization is not only coexisting with magnetic ordering, but it is also induced by the onset of it, which hence implies strong coupling between both ferroic ordering parameters [12]. In many systems the driving mechanism for this effect is the inverse Dzyaloshinskii-Moriya interaction (DMI), for which a spin canting of neighboring spins $\boldsymbol{S}_i$ and $\boldsymbol{S}_j$ induces a ferroelectric polarization, whose direction is defined by $\boldsymbol{P} \propto \boldsymbol{e}_{ij} \times (\boldsymbol{S}_i \times \boldsymbol{S}_i)$ with $\boldsymbol{e}_{ij}$ being the connecting vector of neighboring spins [14–16].

The understanding of the read and write performance under different conditions is indispensable for the development of new memory devices. The control and the dynamics of multiferroic domain inversion were studied intensively for $TbMnO_3$ and $MnWO_4$ using neutron scattering techniques, second-harmonic generation (SHG) measurements, and dielectric spectroscopy [17–21]. The relaxation behavior in both systems differs significantly as a function of temperature and electric-field amplitude [18–20]. In $MnWO_4$ domain inversion speeds up, when cooling towards the lower commensurate magnetic phase [18,21], which is attributed to depinning of multiferroic domains by anharmonic modulations [22,23]. In $TbMnO_3$ the domain inversion can be well described by a remarkably simple law combining an Arrhenius-type activated temperature dependence with a field dependence following the Merz law established for ferroelectrics [20]. In contrast to $MnWO_4$, the incommensurate long-range order in multiferroic $TbMnO_3$ does not transform into a commensurate arrangement [24,25] but is only altered through the additional order of Tb^{3+} moments [26]. Apparently, competing incommensurate and commensurate ordering significantly influence the relaxation behavior of multiferroic domain inversion and thus complicate its description [23]. Therefore, multiferroic materials with simple phase diagrams are desirable for further investigations of multiferroic domain dynamics.

The broad class of pyroxenes with chemical formula $AMeX_2O_6$ with A = Li, Na, Sr, or Ca, X = Si or Ge, and *Me* a magnetic transition metal exhibit several interesting magnetic ordering phenomena, with controllable ferrotoroidicity in $LiFeSi_2O_6$ [27,28] and multiferroic phases in $NaFeSi_2O_6$ [27], in $NaFeGe_2O_6$ [29] and in $SrMnGe_2O_6$ [30] being the most prominent ones. In spite of the similar monoclinic crystal structure with magnetic zigzag chains running along the *c*

*biesenkamp@ph2.uni-koeln.de

†braden@ph2.uni-koeln.de

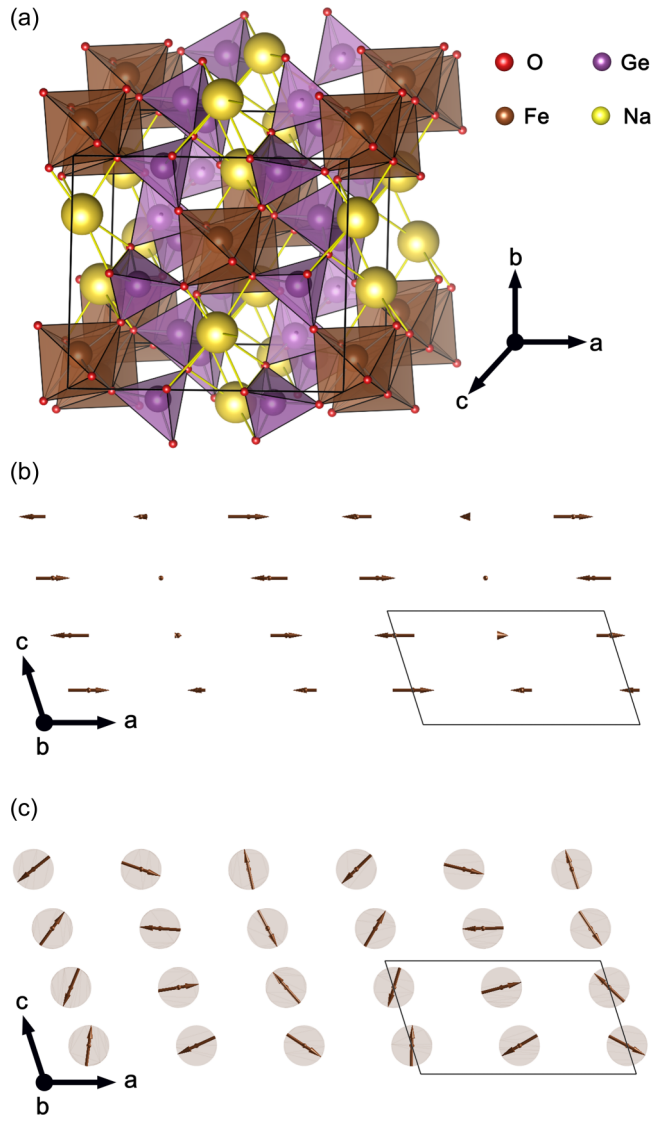

FIG. 1. The nuclear structure (with data from Ref. [35]) is shown in (a) by utilizing the crystallographic visualization software VESTA3 [38]. Both (b) and (c) sketch the magnetic structure of the intermediate SDW phase and of the low-temperature spin-spiral phase, respectively.

direction (see Fig. 1), the multiferroic mechanism is different in these three pyroxenes. In $NaFeSi_2O_6$ two successive transitions involving the same irreducible representation result in a helical structure with the propagation vector along the monoclinic axis [31]. In this material multiferroic order does not result from the spin current or inverse Dzyaloshinski-Moriya mechanism [14–16,32] but from the combination of the chiral order and the monoclinic distortion. In contrast, multiferroic order in $SrMnGe_2O_6$ [30] and in $NaFeGe_2O_6$ [33] seems to follow the most common inverse Dzyaloshinski-Moriya mechanism [14–16,32] but with differently oriented cycloidal and ferroelectric order.

$NaFeGe_2O_6$ exhibits the sequence of two incommensurate ordered phases that is characteristic for many type-II multiferroics, and there is just one magnetic site [29,33–36]. The system crystallizes in the monoclinic space group $C2/c$ with $a = 10.0073(8)$ Å, $b = 8.9382(7)$ Å, $c = 5.5184(4)$ Å, and $\beta = 107.524(1)^\circ$ [35,37]. Edge-sharing FeO_6 octahedra form zigzag chains along the c direction. These chains are separated by corner-sharing GeO_4 tetrahedra that are also stacked along the c axis (see Fig. 1). Below $T \approx 35$ K, short-range ordering was observed and two different magnetic phases with incommensurate long-range order were reported for $NaFeGe_2O_6$ with transition temperatures at $T_N \approx 13$ K and $T_{MF} \approx 11.6$ K [33–36]. First at T_N an incommensurate spin-density wave (SDW) evolves with moments pointing roughly along the a direction [33] and below T_{MF}, spins form a chiral spin structure with moments lying within the ac plane [34,35]. A small b component of the chiral structure was controversially discussed [34,35], and in [35] only a single transition is observed. Simultaneous to the onset of the chiral spin arrangement, a ferroelectric polarization ($\boldsymbol{P} \approx 32\ \mu C\,m^2$) develops [29,36]. The ferroelectric polarization is confined to the ac plane as the given symmetry forbids a nonzero component of the polarization along b [33] (see Sec. III), but symmetry allows for a finite b component of the chiral spin structure.

The absence of a competing commensurate phase makes $NaFeGe_2O_6$ an ideal candidate to investigate multiferroic domain dynamics. In the following sections we will first discuss the presence of the magnetic b component utilizing neutron polarization analysis. Subsequently, we will report on our investigations of multiferroic domain inversion in $NaFeGe_2O_6$. Finally, we will discuss the measured spin-wave velocity, which is proposed to limit the inversion speed of multiferroic domains.

II. EXPERIMENTAL METHODS

A detailed description of the $NaFeGe_2O_6$ single-crystal growth by the top seeding technique can be found in Ref. [36]. For our measurements, two single crystals (SI and SII) were prepared and had been characterized by susceptibility measurements utilizing a commercial superconducting quantum interference device (SQUID) magnetometer. For both samples the transition temperatures are slightly reduced to $T_N \approx 12.5$ K and $T_{MF} \approx 11.1$ K with respect to literature [36]. In order to apply electric fields to the system, both samples were mounted between aluminium plates, which can be connected to a high-voltage setup. The ferroelectric polarization is largest along the a direction [36] and the plate normal was oriented parallel to a^*. The sample surface was thinly coated with silver paste for optimized electric contact and the aluminum plates were tightened together by insulating polytetrafluorethylene (PTFE) screws (see Ref. [20]). The plates that are cramping the respective sample were connected to sample holders defining the scattering geometry (1 0 0)/(0 0 1) for sample SI and (1 0 0)/(0 1 0) for sample SII.

Neutron polarization analysis senses the different components of the magnetic structure and the sign of the vector chirality. The respective experiments were performed at the cold three-axes spectrometer IN12 (located at the Institut Laue-Langevin) and at the cold three-axes spectrometer 4F1 (located at the Laboratoire Léon Brillouin).

At IN12, a horizontally and vertically focusing pyrolytic graphite (002) monochromator supplied $\lambda = 3$ Å and a supermirror cavity provided a highly polarized neutron beam

(flipping ratio of about FR ≈ 4). Higher-order contaminations were suppressed by a velocity selector. The IN12 spectrometer was also equipped with a Helmholtz-coil setup in order to define the guide-field direction at the sample position, and spin flippers before and after the sample position enabled longitudinal polarization analysis. A curved Heusler (111) analyzer selected the final beam polarization. For studying the multiferroic domain distribution we used the full polarization analysis, although these experiments can also be performed in a half-polarized mode. However, the full analysis yields a better background. The correction for finite neutron polarization was done following [39], whereby due to the high total flipping ratio the impact of this correction is negligible.

In the absence of external electric fields, the multiferroic polarization and the chirality of the magnetic structure will not be uniform, but domains with opposite polarization and chirality will form. Multiferroics can, however, be poled by cooling in large external electric fields applied along the ferroelectric polarization [22,40,41] resulting in an almost monodomain state. In our experiments on $NaFeGe_2O_6$ we always applied the external electric field along the a^* direction.

A conventional high-voltage generator (FUG HCP 14-3500) was deployed for measurements with quasistatic electric fields ($|U| \leqslant 3.5\,\mathrm{kV}$) but a stroboscopic high-voltage setup was used for the time-resolved investigation of the multiferroic domain relaxation. This setup contains two high-voltage modules (ISEG BPP4W and ISEG BPN4W) providing high voltage ($|U| \leqslant 4\,\mathrm{kV}$) with opposite polarity and a fast MOSFET array (BEHLKE HTS-111), which is capable to switch the high-voltage output polarity with 50 μs [20]. For $TbMnO_3$ rapid electric-field-driven relaxation was indeed observed at these timescales [20].

A multichannel data collector (MESYTEC MCPD-8) records all detector events as well as a synchronization signal, when the polarity of the applied electric field is switched. All events are recorded together with a time stamp, which allows one to periodically switch the field, while summing the detected neutrons in time bins with respect to the moment when the field is reversed. This stroboscopic method thus enables one to investigate very fast relaxation processes because the width of each time bin can be arbitrarily selected, while repeating the switching periodically yields the required statistics. The time resolution is limited by the finite spreads of neutron velocities and path lengths. Reference [20] gives a detailed description of this setup and of the stroboscopic technique.

For long relaxation times above several minutes, the counting statistics obtained during a single switching period is sufficient and does not require the stroboscopic setup. The respective measurements of long relaxation times were performed at the cold three-axes spectrometer 4F1. A double pyrolytic graphite monochromator setup supplied $\lambda = 4.2$ Å and a supermirror bender polarized the neutron beam (flipping ratio of about FR ≈ 50). For polarization analysis, a MuPad system [42] and a horizontally curved Heusler analyzer were installed. In order to measure the spin-wave velocity, a polarized beam is not required and the respective experiment was conducted at the 4F2 spectrometer. The double pyrolytic-graphite monochromator provided an unpolarized neutron beam with $\lambda = 4.05$ Å and the pyrolytic-graphite analyzer enables inelastic measurements, for which a cooled Be filter was additionally inserted.

III. MAGNETIC STRUCTURE

So far, the magnetic structure of $NaFeGe_2O_6$ was not yet fully characterized as a b component of the chiral spin structure was controversially discussed [34,35] and as the reported determination of the intermediate structure was only based on neutron powder diffraction experiments [33,34]. The neutron polarization analysis on single crystals permits a precise separation of magnetic components and unambiguous identification of chiral signatures.

The symmetry conditions of incommensurate magnetic order with a propagation vector $\boldsymbol{k} = (k_h\, 0\, k_l)$ have been discussed for $NaFeGe_2O_6$ in Ref. [33]; they are furthermore identical to those in multiferroic $LiFe(WO_4)_2$ [43,44]. In space group $C2/c$ only one symmetry element has to be considered, the glide-mirror plane c, which transforms (m_x, m_y, m_z) into $(-m_x, m_y, -m_z)$. Therefore, it is obvious that magnetic x, z, and y components are separated. The character concerning this c element is ± 1 up to the phase correction. The inverse of this phase enters the basis vector components for the second site. In the magnetic superspace group formalism all magnetic moments are developed in cosine and sine series starting from the atoms in the primitive unit cell. Here we have two magnetic ions in the unit cell and the coefficients of these two are not independent but determined through the condition that the moment at $-\mathbf{r}$ and $-x_4$ (the argument of the modulation functions) is identical to the moment at $\mathbf{r}$ and x_4, which is just the inversion symmetry [45]. Therefore, only one set of cosine and sine functions is required in the harmonic description. For one-dimensional irreducible representations, as it is the case here, there is a one-to-one correspondence between irreducible representation and magnetic superspace group formalisms, but the representation analysis leaves the phases undefined, while magnetic superspace group analysis fixes these phases, leaving only three free parameters for each of the magnetic modes [45]. The symmetry of the two different incommensurate magnetic modes is given in Table I.

The magnetic superspace group analysis explains that a multiferroic cycloid cannot be obtained with a single symmetry mode, as the inversion symmetry is not broken [45]. One may also argue that in each of the two modes, the x and z components are modulated in phase, while x, z, and y components have a different character between the two sites so that any spin-current contributions cancel out, as it is also the case in the intermediate phase in $MnWO_4$ [46]. In order to generate cycloidal order, one needs to couple two magnetic modes with a phase shift of $(\frac{\pi}{2} + n\pi)$ by either combining the two different magnetic modes or by combining twice the same mode with the phase shift. In the former case, the glide-mirror symmetry is lost and ferroelectric order appears along the b direction as in $LiFe(WO_4)_2$ [43,44], while in the latter case the mirror plane persists and enforces ferroelectric polarization in the a, c plane [33]. This is the situation in the multiferroic phase of $NaFeGe_2O_6$.

Magnetic scattering will only arise from magnetic components perpendicular to the scattering vector and spin-flip (SF) processes necessitate a component of the magnetization

TABLE I. Symmetry conditions for the two incommensurate magnetic modes that can appear for a propagation vector $\boldsymbol{k} = (k_h\ 0\ k_l)$ in the space group $C2/c$ with a single magnetic ion at (0,0.904,0.25). The conditions are defined by the irreducible representation Γ_1 and Γ_2 and the corresponding basis vectors for the two Fe sites are given with $a = e^{i2\pi\delta\mathbf{r}\mathbf{q}_{\mathrm{inc}}}$. Here $\delta\mathbf{r} = \mathbf{r}_2 - \mathbf{r}_1$ and $a^* = 1/a$ is the complex conjugate of a. Representation analysis and superspace group formalism are equivalent in the case of $NaFeGe_2O_6$, but the superspace group formalism fixes the phases between modulations so that for each of the two modes the magnetic structure is described by only three parameters corresponding to either cosine or sine modulations. The resulting superspace groups for a single mode are given in the last column.

Γ	1	c	(x, y, z)	$(x, \bar{y}, z + 1/2)$	Coefficients	Character	Superspace group
Γ_1	1	$-a$	(u, v, w)	$a^*(u, -v, w)$	Re(u)Im(v)Re(w)	cos/sin/cos	$C2/c1'(\alpha 0 \gamma)0ss$
Γ_2	1	a	(u, v, w)	$a^*(-u, v, -w)$	Im(u)Re(v)Im(w)	sin/cos/sin	$C2/c1'(\alpha 0 \gamma)00s$

perpendicular to the direction of the incoming beam polarization. In contrast, non-spin-flip (NSF) processes only sense components that are aligned parallel or antiparallel to the incoming neutron beam polarization. This allows one to distinguish the different components of the $\boldsymbol{Q}$th Fourier component of the magnetization density given by

$$\boldsymbol{M}(\boldsymbol{Q}) = \int \boldsymbol{M}(\boldsymbol{Q})\exp(i\boldsymbol{Q}\boldsymbol{r})d^3r. \tag{1}$$

For neutron polarization analysis it is convenient to define a right-handed coordinate system, where the x direction is set parallel to the scattering vector $\boldsymbol{Q}$, y is perpendicular to x but confined to the scattering plane, and z is perpendicular to both x and y. I_{ij} denotes the scattering intensity for the neutron polarization changing from i to j with $i, j = x, y, z, \bar{x}, \bar{y}, \bar{z}$ (the overbar signifies antiparallel polarization). With the longitudinal polarization setup, only the diagonal terms are accessible.

During the first part of the allocated beam time at IN12, sample SI with scattering geometry (1 0 0)/(0 0 1) was mounted. Both components of the incommensurate propagation vector $\boldsymbol{k} = (k_h\ 0\ k_l)$ could be traced as a function of temperature. For the respective measurements, Q_h and Q_l scans were executed across the magnetic reflection $\boldsymbol{Q} = (0.678\ 0\ -1.075)$ and each Q scan was fitted by a Gaussian function. Exemplary scans for different SF channels are shown in Fig. 2. It can be seen that the crystal is twinned, which, however, does not affect the following analysis as consistently only the peak from the same twin was considered during the experimental courses. The observed peak center values were considered for defining the scan of the following step in temperature. Figures 2(c) and 2(d) display the obtained temperature-dependent values for k_h and k_l, and it can be seen that both components vary with temperature but lock in a constant value at $T \approx 5$ K. The results qualitatively agree with the reported temperature dependence of the incommensurate propagation vector in Ref. [35].

The used scattering geometry entails that the SF channels are described by $I_{\bar{y}y} \propto M_b M_b^*$ and $I_{\bar{z}z} \propto M_{ac}M_{ac}^*\sin^2(\alpha)$ with M_b and M_{ac} being the complex Fourier components of the magnetization along b direction and within the ac plane, respectively, and $\sin^2(\alpha)$ being the geometry factor. a and a^* are not parallel in the monoclinic system, but in the used scattering geometry both are lying within the scattering plane. The same holds for c and c^*. Due to the incommensurability of the magnetic structure, no nuclear signal contributes to the measured intensity. The SF channels $I_{\bar{x}x}$ and $I_{x\bar{x}}$ are described by

$$I_{\bar{x}x}, I_{x\bar{x}} \propto \boldsymbol{M}_\perp\boldsymbol{M}_\perp^* \pm i(\boldsymbol{M}_\perp \times \boldsymbol{M}_\perp^*)_x, \tag{2}$$

with $\boldsymbol{M}_\perp$ the projection of the Fourier component $\boldsymbol{M}(\boldsymbol{Q})$ perpendicular to the scattering vector, but as the scattering vector

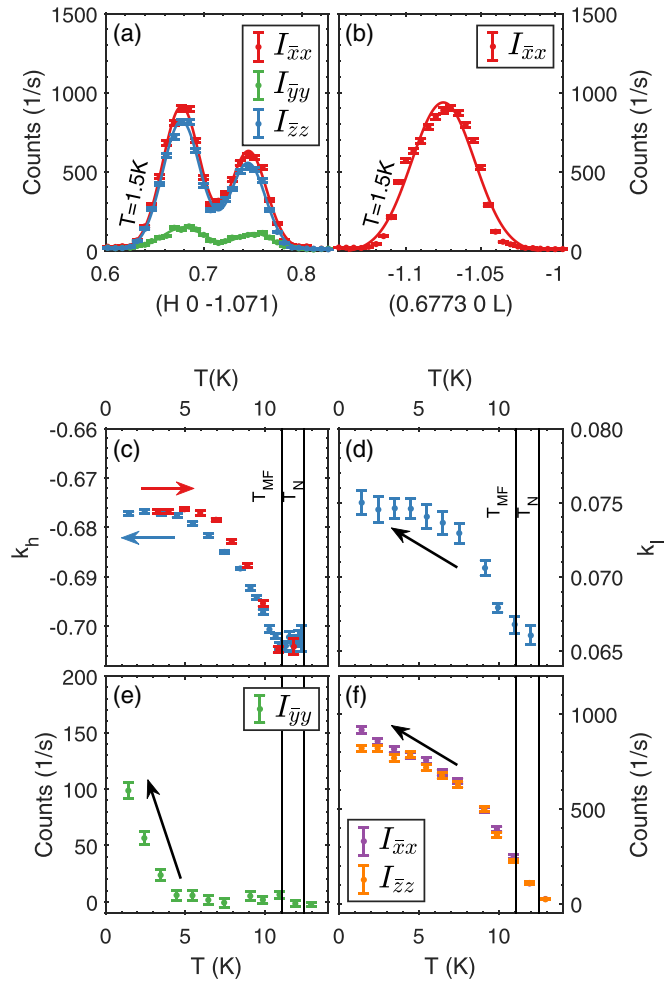

FIG. 2. (a), (b) Display exemplary Q_H and Q_L scans for different SF channels. The temperature-dependent components k_h and k_l of the propagation vector $\boldsymbol{k} = (k_h\ 0\ k_l)$ are, respectively, shown in (c) and (d). The blue and red data correspond to cooling and heating sequences, respectively. In (e) and (f) the peak intensity of reflection $\boldsymbol{Q} = (0.678\ 0\ -1.075)$ is plotted for all SF channels as function of temperature. All intensities were corrected for the finite flipping ratio and all measurements were performed on sample SI.

lies within the basal plane of the chiral spin structure the chiral term vanishes. The intensity of all three SF channels is plotted in Figs. 2(e) and 2(f). It can be clearly seen in Fig. 2(c) that $I_{\bar{y}y}$ exhibits finite intensity only below $T \approx 5\,\mathrm{K}$ thus indicating the development of a finite b component of the magnetic structure within the multiferroic phase of $NaFeGe_2O_6$, but exclusively at low temperature. The onset of this component coincides with the lock-in temperature of the incommensurate propagation vector. Figure 2(f) shows that below the first transition at T_N, the total magnetic scattering signal $I_{\bar{x}x}$ initially features the same amplitude as $I_{\bar{z}z}$, which senses the magnetic moments within the ac plane. This confirms that the magnetic structure is first confined to the ac plane until below $T \approx 5\,\mathrm{K}$ the discrepancy between $I_{\bar{z}z}$ and $I_{\bar{x}x}$ also indicates the evolving b component of the magnetic structure. From this difference the magnitude of the b component can be estimated. A single-crystal refinement yielded $4.09(4)\mu_B$ [35] for the total magnetic moment and when considering a perfect circular spiral, the averaged moment along the principal axis becomes $4.09/\sqrt{2}\mu_B \approx 2.89\mu_B$. Its square value is sensed by $I_{\bar{x}x}$ and as $I_{\bar{y}y} \propto m_b^2$ is approximately 10% of $I_{\bar{x}x} = I_{\bar{y}y} + I_{\bar{z}z}$ [see Figs. 2(e) and 2(f)], the magnetic component along b direction can be estimated to $m_b \approx \sqrt{0.1 \times 2.89^2}\mu_B \approx 0.89\mu_B$. The developing b component agrees with the discussed and underlying superspace symmetry, which confines the electric polarization to the ac plane [33].

Sample SII was mounted with scattering geometry (1 0 0)/(0 1 0) and no twinning was observed for this specimen. In this configuration the SF channels $I_{\bar{y}y}$ and $I_{\bar{z}z}$ sense the magnetization along the c direction and within the a^*, b plane, respectively. The magnetic reflection $\boldsymbol{Q} = (0.32\ 3\ 0.08)$ is not directly accessible within the given scattering plane but the finite l value can be reached by tilting the goniometer by $\approx 3^\circ$, which does not have significant impact on the analysis of respective SF and NSF channels. The temperature dependence of both SF channels is plotted in Fig. 3(a) and it is visible that the c component of the magnetic structure mainly develops below the second transition T_{MF} but, nevertheless, finite intensity and thus a nonzero component along c is also present in the intermediate phase. The chiral spin structure in the multiferroic phase thus exhibits moments in the ac plane with an additional b component, which develops below $T \approx 5\,\mathrm{K}$. In the intermediate phase between $T_N = 12.5\,\mathrm{K}$ and $T_{MF} = 11.1\,\mathrm{K}$ the SF channel $I_{\bar{z}z}$ possesses extensive intensity compared to $I_{\bar{y}y}$ and as the angle between $\boldsymbol{Q}$ and b amounts to approximately 6.9°, the SF channel $I_{\bar{z}z}$ essentially senses the component parallel to a^* [note that $\sin^2(6.9^\circ) \approx 0.014$]. With results from both scattering geometries it can be concluded that the SDW structure exhibits moments $\boldsymbol{m}$ that are lying essentially in the a, c plane and we determine this angle by

$$\measuredangle(\boldsymbol{m}, \boldsymbol{a}^*) = \tan^{-1}\left(\frac{m_c}{m_{a^\star}}\right) \approx \tan^{-1}\left(\sqrt{\frac{I_{\bar{y}y}}{I_{\bar{z}z}}}\right) \qquad (3)$$

to amount to $\approx 17^\circ$.

The scattering vector in the scattering configuration of sample SII is almost perpendicular to the basal plane of the chiral structure. Therefore, the chiral term $\pm i(\boldsymbol{M}_\perp \times \boldsymbol{M}_\perp^*)_x$ is finite and contributes to both SF channels $I_{x\bar{x}}$ and $I_{\bar{x}x}$ with a different sign. Hence, the sum and the difference of $I_{x\bar{x}}$ and $I_{\bar{x}x}$ are given by $2\boldsymbol{M}_\perp\boldsymbol{M}_\perp^*$ and by the absolute value of $-2i(\boldsymbol{M}_\perp \times \boldsymbol{M}_\perp^*)_x$, respectively. Both the sum and the difference of $I_{x\bar{x}}$ and $I_{\bar{x}x}$ are plotted in Fig. 3(b) as a function of temperature and it can be seen that the chiral signal develops only below T_{MF} within the multiferroic phase. The chiral ratio is defined as

$$r_\chi = (I_{x\bar{x}} - I_{\bar{x}x})/(I_{x\bar{x}} + I_{\bar{x}x}) \qquad (4)$$

and for a monodomain sample it corresponds to $\pm i(\boldsymbol{M}_\perp \times \boldsymbol{M}_\perp^*)_x/|\boldsymbol{M}_\perp|^2$, the ratio of the chiral part with respect to the overall magnetic scattering contribution. The chiral ratio amounts to ± 1 only for a completely poled multiferroic state with ideal geometry. However, as the scattering vector $\boldsymbol{Q}$ is not perfectly oriented perpendicular to the rotation plane of spins, and due to ellipticity the chiral ratio remains below one. In Fig. 3(c) the chiral ratio is plotted and it can be seen that even in the absence of an applied electric field, the chiral ratio possesses a finite value within the multiferroic phase and thus indicates an unbalanced domain distribution of multiferroic domains [22,44]. The quasistatic control of the chiral handedness and the multiferroic domain population by external electric fields is discussed in the following section.

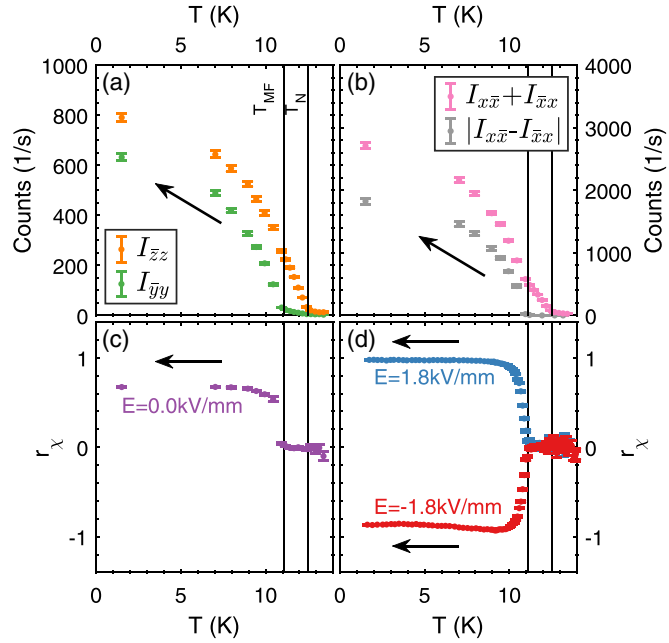

FIG. 3. Polarized neutron scattering in (1 0 0)/(0 1 0) geometry. The temperature dependence of SF channels measured at $\boldsymbol{Q} = (0.32\ 3\ 0.08)$ is shown in (a) and (b). The Q-space position was adjusted with the determined temperature-dependent values of the incommensurate propagation vector [see Figs. 2(c) and 2(d)]. In both (c) and (d) the chiral ratio is plotted as a function of temperature and for different electric-field amplitudes applied along $a^\star$.

IV. QUASISTATIC CONTROL OF MULTIFERROIC DOMAINS

A static electric field with $|E| = 1.8\,\mathrm{kV\,mm^{-1}}$ was applied, while cooling the sample. The chiral ratio was measured simultaneously and its temperature dependence is shown in

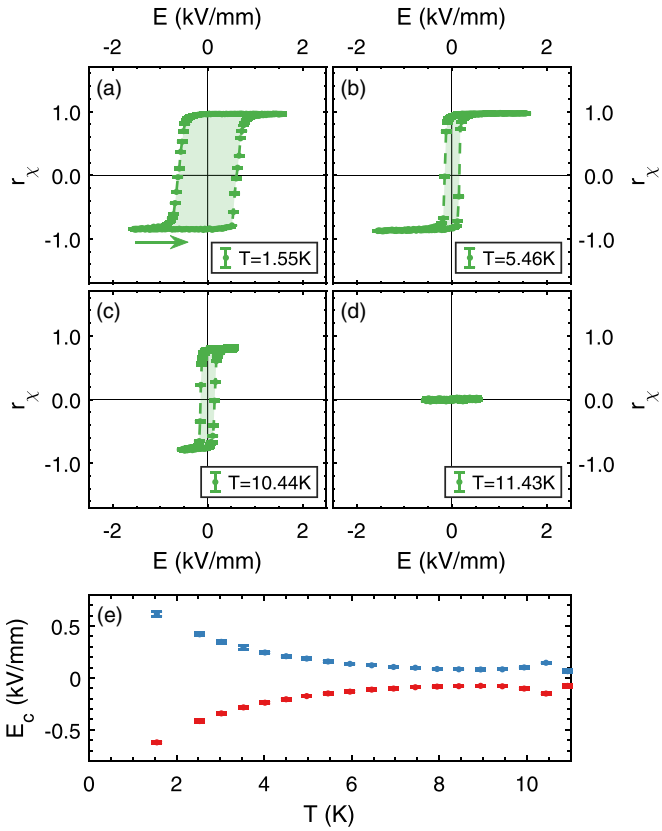

FIG. 4. All recorded hysteresis loops of the chiral ratio shown in (a)–(d) were obtained by driving the applied external electric field (along $a^\star$) slowly (with a period duration of about 45 min) between the two polarities. Both slopes of each hysteresis loop were fitted by a hyperbolic tangent in order to estimate the values of respective coercive fields, which are plotted in (e).

Fig. 3(d) for both field polarities. It can be seen that the chiral ratio reaches the maximum values of $\approx \pm 1$ already slightly below T_{MF}, which indicates a completely poled multiferroic domain distribution and a circular cycloid. This result illustrates the power of polarized neutron diffraction to solve chiral structures, as only the combination of twice the same magnetic mode can cause a chiral signal in this configuration. The chiral phase in $NaFeG_2O_6$ thus must arise from a single irreducible representation similar to $NaFeSi_2O_6$ [31] but the orientation of the propagation vector differs. An opposite-field polarity entails a reversed chiral ratio and an equivalent temperature dependence documenting the controllability of multiferroic domains with applied electric fields in $NaFeGe_2O_6$. The behavior does not significantly change when lowering the field amplitude to $|E| = 1.2\,\mathrm{kV\,mm^{-1}}$ and $|E| = 0.6\,\mathrm{kV\,mm^{-1}}$. In order to quantify the respective values and the temperature dependence of the electric-field amplitude that is needed to reverse the chirality, quasistatic hysteresis loops have been recorded.

Figure 4 displays hysteresis loops of the chiral ratio for different temperatures. The electric field was driven quasistatically between the two polarities corresponding to a period of about 45 min for the entire hysteresis loops and $I_{x\bar{x}}$ and $I_{\bar{x}x}$ were recorded at each field value. The sign of the vector chirality is invertible down to the lowest temperature at $T = 1.55$ K. While approaching the transition to the intermediate phase, the saturation value of the chiral ratio shrinks slightly and abruptly vanishes, when heating above the multiferroic transition. This was also observed by the cooling sequences with applied static fields [see Fig. 3(d)]. The coercive fields that are needed to invert the sign of the chiral ratio in positive or negative direction were determined by fitting both slopes of the hysteresis loops with a hyperbolic tangent. The obtained coercive fields are plotted in Fig. 4(e) as a function of temperature. The coercive fields exhibit a symmetric temperature dependence with the smallest values close to the multiferroic transition.

V. MULTIFERROIC DOMAIN RELAXATION

In order to investigate the relaxation of multiferroic domains in $NaFeGe_2O_6$, while triggering the inversion of domains by external electric fields, the stroboscopic setup was installed at IN12 (see Sec. II). The switching curves of the chiral ratio were recorded for different temperatures and a variety of electric-field amplitudes on sample SII. For each data set with fixed temperature and electric field, we recorded the $I_{x\bar{x}}$ and $I_{\bar{x}x}$ channels as a function of the temperature offset with respect to the field inversion. Figure 5 displays six exemplary switching curves and it can be seen by comparing the panels horizontally that the relaxation time significantly decreases when increasing the temperature. Moreover, the vertical arrangement of panels in Fig. 5 displays the field dependence of the relaxation processes. It can be seen that the electric-field strength at fixed temperature also strongly influences the relaxation processes. For all recorded curves, there is no asymmetric relaxation behavior concerning the electric field polarity.

The relaxation process can be described by an exponential relaxation in both directions [20]:

$$r_\chi(t) = r_a - (r_a - r_b)\exp\left[-\left(\frac{t}{\tau_a}\right)^{b_1}\right], \tag{5}$$

$$r_\chi(t) = r_b - (r_b - r_a)\exp\left[-\left(\frac{t - t_{1/2}}{\tau_b}\right)^{b_2}\right]. \tag{6}$$

Both parameters τ_a and τ_b are the characteristic relaxation times describing the inversion of the chiral ratio from r_a to r_b and from r_b to r_a, respectively. Here, $t_{1/2}$ accounts for the reversal of the electric field after half the period. Considering the Ishibashi-Takagi theory, which is based on the Avrami model, the stretching exponents b_1 and b_2 describe the dimensionality of the domain wall motion [47–51]. Both stretching exponents vary between 1 and 2.5, thus indicating low-dimensional domain growth. Approaching T_{MF} or enhancing the field amplitude result in larger stretching exponents, suggesting a higher growth dimensionality or possibly additional nucleation processes. A similar behavior was observed for $TbMnO_3$ [20].

The investigation of long relaxation times (>1 min) does not require the stroboscopic setup, as sufficient statistics are reached during a single switching period. The respective measurements were performed at 4F1. Two switching curves are exemplarily shown in Fig. 6 for an electric-field

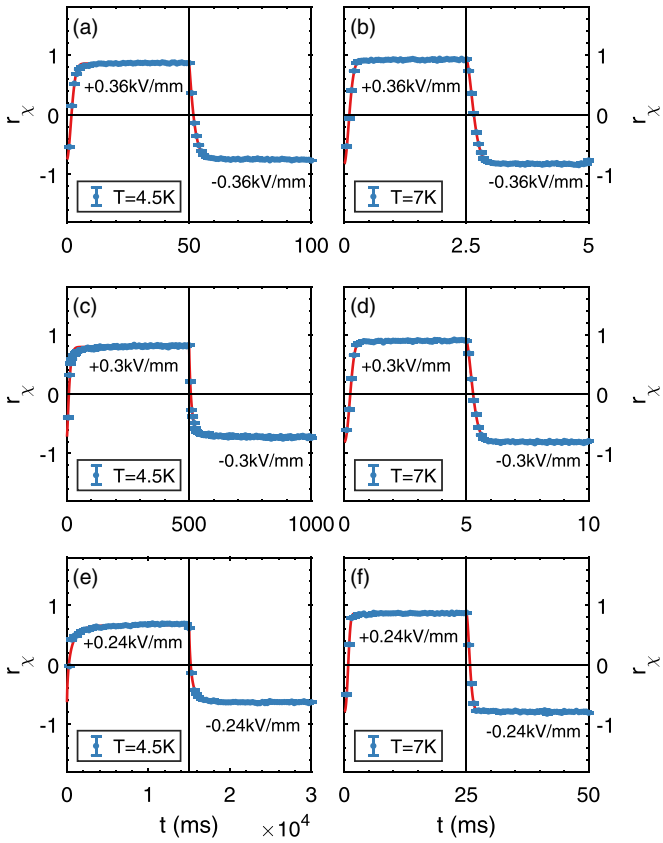

FIG. 5. All displayed switching curves in (a)–(f) were recorded by utilizing the stroboscopic method at IN12 and by measuring on sample SII. The blue data points refer to the recorded chiral ratio and the red line corresponds to the fit. The time dependence of the applied electric field follows a rectangular shape with inversion at the beginning and in the middle of each panel.

amplitude of $|E| = 0.12\,\mathrm{kV\,mm^{-1}}$. Although the experiment was performed on the same sample SII, the curves exhibit an asymmetric relaxation behavior contrary to the recorded curves from the IN12 experiment. The system was short circuited at room temperature and during the cooling procedure but nevertheless this asymmetry can be due to residual frozen-in charges or from effective pinning at defects, which provoke a preferred sign of the vector chirality in the multiferroic phase [22]. Moreover, both curves possess a kink after the second field inversion, which can be related to a time-delayed second nucleation process. However, this effect was resolvable only for the several orders of magnitude slower relaxation processes that were investigated during the 4F1 beamtime.

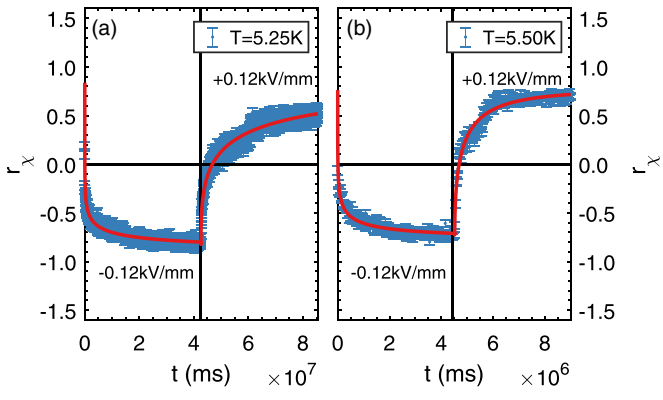

FIG. 6. At 4F1 the relaxation processes of the chiral ratio, which is plotted in (a) and (b), were recorded by counting both SF channels $I_{x\bar{x}}$ and $I_{\bar{x}x}$ as a function of time. The electric field ($|E| = 0.12\,\mathrm{kV\,mm^{-1}}$) was manually switched after the saturation of the chiral ratio for the respective handedness was reached. For both curves, sample SII was measured.

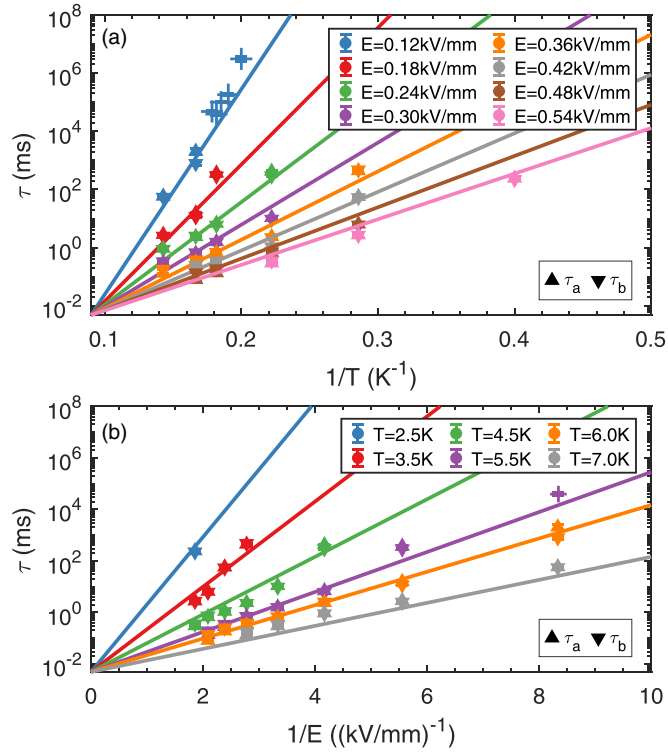

FIG. 7. (a), (b) Display the temperature- and electric-field-dependent relaxation times, respectively. Up and down triangles refer to τ_a and τ_b from IN12 data, whereas crosses correspond to τ_a from the recorded 4F1 data. The whole IN12 data set was fitted simultaneously by the combined Arrhenius-Merz law [see Eq. (7)] and the plotted colored solid lines refer to the fit results shown for fixed electric fields in (a) or fixed temperatures in (b). The 4F1 data were not included to the fit.

Figure 7 displays the fitted relaxation times τ_a and τ_b [see Eqs. (5) and (6)] as a function of inverse temperature and of inverse field with a logarithmic scaling. Up and down arrows mark the fitted relaxation time from IN12 data for switching the electric field to positive and negative values, respectively. The crosses in Figs. 7(a) and 7(b) mark the fitted relaxation times, which have been obtained from the 4F1 experiment. Combining both experiments at IN12 and 4F1 it is possible to follow the multiferroic relaxation over seven orders of magnitude in time as a function of temperature and electric field.

The multiferroic domain relaxation in $TbMnO_3$ [20] follows a combined Arrhenius-Merz law as a function of temperature and electric field:

$$\tau(E,T) = \tau^* \exp\left(\frac{A_0 T_r}{ET}\right) \quad \text{with } T_r = \frac{T_{\mathrm{MF}} - T}{T_{\mathrm{MF}}}. \tag{7}$$

Here τ^* denotes the fastest possible relaxation time that can be reached at the multiferroic phase transition T_{MF} or at infinitely large fields, and A_0 is the activation constant. Thus, τ^* and A_0 are the only two parameters needed to describe the field and temperature dependence of the relaxation. For $TbMnO_3$ the parameters amount to $\tau^* = 0.72\,\text{ms}$ and $A_0 = 1483\,\text{K kV mm}^{-1}$ [20]. This combined Arrhenius-Merz relation describes multiferroic relaxation in the E,T range, where it is determined by classical domain wall motion. In the studied E, T range, the multiferroic relaxation in $TbMnO_3$ deviates from the combined Arrhenius-Merz law only when approaching the multiferroic transition, as additional nucleation processes seem to accelerate the domain inversion.

For $NaFeGe_2O_6$ all relaxation times obtained from IN12 data were simultaneously fitted with the combined Arrhenius-Merz law. The 4F1 data were excluded from the fit as even a tiny temperature offset between both instruments due to different sample sticks and temperature calibration has significant impact on the fit result. Furthermore, the asymmetry of relaxation and the second nucleation process complicate the precise determination of relaxation times. Nevertheless, the temperature- and electric-field-dependent relaxation times τ_a from 4F1 data are included in Fig. 7 (see crosses). Due to the observed asymmetry for long relaxation times only τ_a is plotted, whereas τ_b is approximately one order of magnitude larger.

Solid lines in Figs. 7(a) and 7(b) correspond to the fit result for different temperatures and different electric-field amplitudes. It is clearly visible that the multiferroic relaxation behavior in $NaFeGe_2O_6$ is also well described by this combined activation law requiring only two parameters. The obtained critical relaxation time τ^* and the activation constant A_0 amount to $\tau^* = 0.0049(12)\,\text{ms}$ and $A_0 = 19.5(9)\,\text{K kV mm}^1$. Both values are much smaller than those observed in $TbMnO_3$ [20]. The roughly two orders of magnitude smaller τ^* value indicates a faster domain wall motion in $NaFeGe_2O_6$ which will be shown below to be consistent with the spin-wave velocity. The slower processes in $TbMnO_3$ can stem from the pronounced ellipticity of the chiral structure that implies anharmonicities and damping of the magnetic excitations [52]. The smaller activation parameter in $NaFeGe_2O_6$ indicates less pinning of the multiferroic order, which can be attributed to the much lower value of the ferroelectric polarization compared to $TbMnO_3$ [36].

During a second experiment at the IN12 spectrometer, the relaxation times at very low temperatures were further studied. Before this beam time, a tiny piece was cut from sample SII for other measurements and the sample contacts were renewed. With the restored sample setup a slightly different critical relaxation time and activation constant was observed but nevertheless both values [$\tau^* = 0.0125(18)\,\text{ms}$ and $A_0 = 13.28(34)\,\text{K kV mm}^{-1}$] are of the same order of magnitude compared to results from the first experiment. The measured relaxation times as well as the fit are shown in Fig. 8, and it can be seen that even at low temperature the relaxation follows the activation law indicating that no quantum effects dominate the relaxation behavior, which would lead to a saturation of the relaxation time. For fields between $E = 0.42\,\text{kV mm}^{-1}$ and $1.02\,\text{kV mm}^{-1}$, the domain wall motion in $NaFeGe_2O_6$ remains thus thermally activated and is not driven by domain wall tunneling down to $T = 1.5\,\text{K}$. Domain wall tunneling was reported for magnetic and ferroelectric domain wall motion at low temperature [53–55]. In $NaFeGe_2O_6$, quantum effects can become relevant at even lower temperature and electric field values.

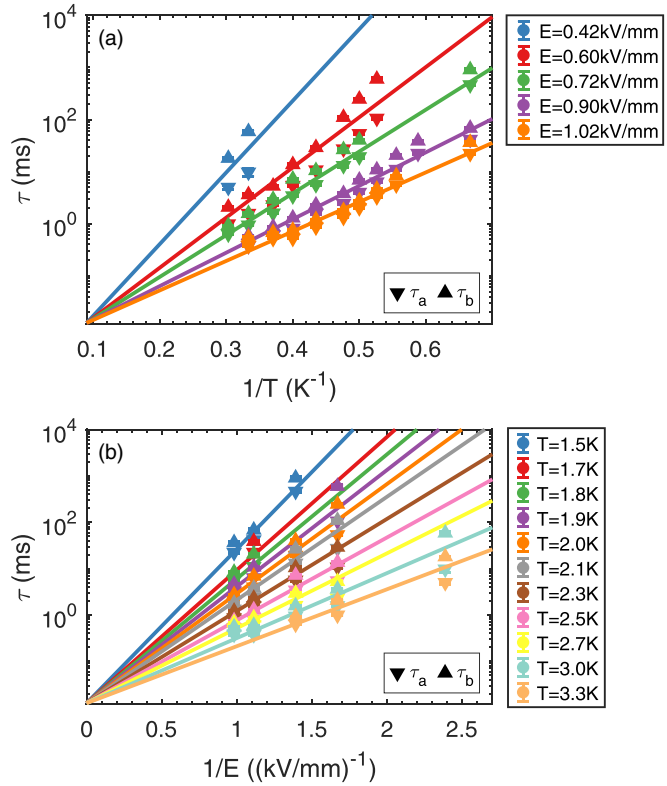

FIG. 8. Additional set of measurements of the relaxation times from a second experiment are displayed in (a) and (b). The combined Arrhenius-Merz law is valid even at very low temperatures. A slightly different activation constant and critical relaxation time with respect to results shown in Fig. 7 arise from a renewed sample setup (see text).

Some pure ferroelectrics [56,57] exhibit thermally activated relaxation following a scaling law $\tau(E, T) = \tau^* \exp(A_0 T_r / E)$, in which the relaxation only depends on the ratio T_r/E. The measurements on multiferroic $TbMnO_3$ [20] do not agree with this but follow a scaling with $T_r/(ET)$ as it results from the combined Arrhenius-Merz law. Figure 9 compares both scaling laws for $NaFeGe_2O_6$ and clearly shows that the combined Arrhenius-Merz law is the appropriate scaling description also for this material.

The relaxation of multiferroic domains differs from the relaxation behavior in conventional ferroelectrics [20,56,57]. In a ferroelectric material the nucleation process, the forward growth, and the subsequent sideways expansion of domains can equally contribute to the global domain relaxation process and thus render its description complicated [56,57]. In contrast, multiferroic domain inversion is dominantly determined by the slow sideways growth of domains [19,20,58,59]. Therefore, thermally activated domain wall motion and a combined Arrhenius-Merz law [20] describe the multiferroic domain inversion over a wide range of temperatures and fields, spanning over seven orders of magnitude in time. However, close to

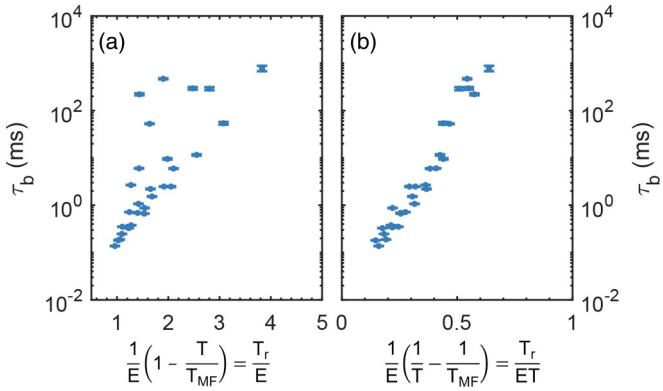

FIG. 9. The different scaling relations for the relaxation times shown in (a) and (b) clearly determine the combined Arrhenius-Merz law to be the correct description of the multiferroic domain inversion. For the comparison only IN12 data from the first experiment (see Fig. 7) were used.

the multiferroic transition and for very high fields, additional nucleation processes will accelerate the relaxation, and at very low temperatures and electric fields quantum tunneling can become relevant.

VI. SPIN-WAVE VELOCITY

Since the spin-wave velocity can limit the multiferroic domain wall motion [19,20] we analyzed the dispersion of acoustic magnon branches at the 4F2 triple-axis spectrometer. The respective measurements were carried out on sample SI, which was mounted with scattering geometry (1 0 0)/(0 0 1). For $\Delta E \geqslant 0.5\,\mathrm{meV}$, constant-energy scans were measured around the incommensurate zone center $\boldsymbol{Q} = (0.677\ 0\ 0.925)$ along H and L directions at $T = 3.9\,\mathrm{K}$. Below $\Delta E = 0.5\,\mathrm{meV}$ it was not possible to separate the excitation from the elastic line due to the finite resolution. Figure 10 maps the measured scattering along both recorded directions. Respectively, two exemplary constant-energy scans are shown in Figs. 10(a) and 10(b). All constant-energy scans were fitted with two Gaussian functions and the obtained peak-center positions of excitations are marked by red data points in Figs. 10(c) and 10(d). The dispersion can be approximately described by $\omega(q) = \sqrt{(\Delta^2 + v_g^2 q^2)}$, with v_g the group velocity of the spin wave and Δ the gap energy. The fits for respective directions (red dashed lines in Fig. 10) yield $v_g = 662(19)\,\mathrm{m\,s^{-1}}$ along H, $v_g = 1460(36)\,\mathrm{m\,s^{-1}}$ along L and a spin gap of approximately 0.5(2) meV for both directions. The magnon dispersion is thus anisotropic with a steeper slope along the direction of zigzag chains, but this anisotropy is moderate and the material should not be considered as a low-dimensional system.

We have calculated the spin-wave dispersion using the SPINW code [60], for which the result is shown in Fig. 11. So far, only for the pyroxene $SrMnGe_2O_6$ a quantitative study of the magnon dispersion was reported [61] but this material exhibits already a different orientation of the propagation vector. We follow this $SrMnGe_2O_6$ model, which takes three interaction parameters into account: the nearest-neighbor coupling J within the zigzag chains (distance 3.25 Å), the nearest

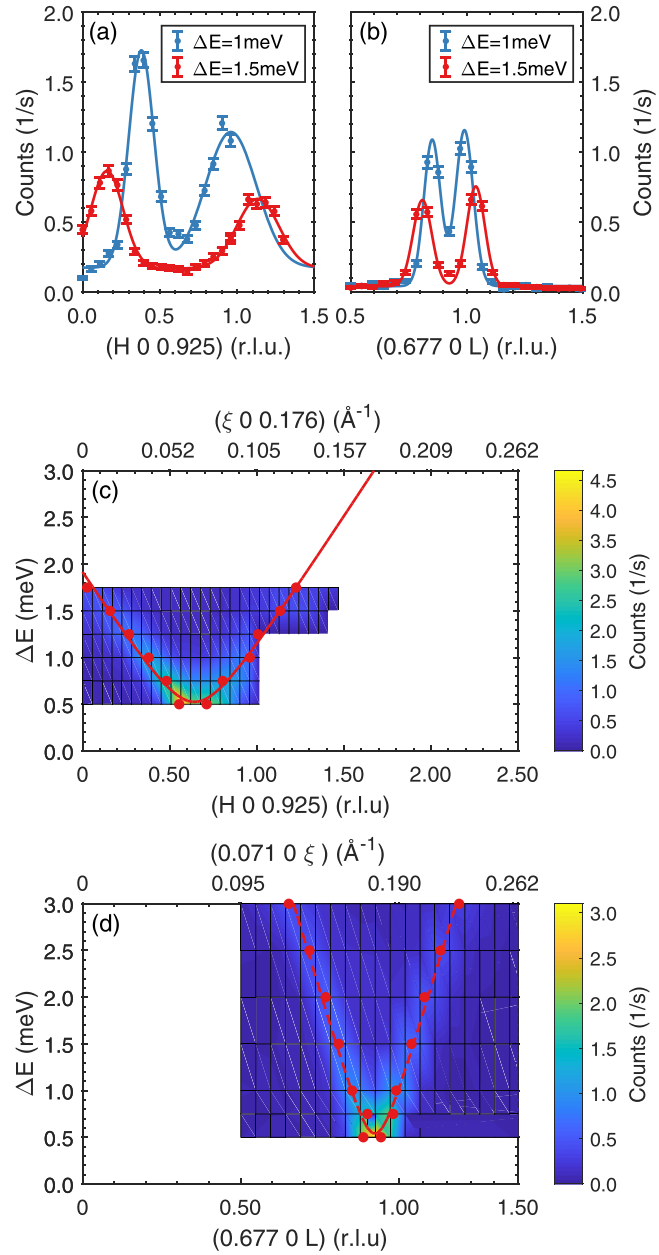

FIG. 10. The plots in a) and b) display exemplary two recorded constant-energy scans at $T = 3.9\,\mathrm{K}$ around the incommensurate zone center $\boldsymbol{Q} = (0.677\ 0\ 0.9252)$ along H and L, respectively. Both panels c) and d) show the complete measured data sets, whereby red data points refer to the fitted peak maxima and the red lines correspond to fits of the respective dispersion.

interchain coupling J_1 (distance 5.64 Å), and the next-nearest interchain coupling J_2 [distance 6.70 Å corresponding to the (0.5 0.5 0) C translation]. All parameters correspond to the exchange interaction per bond. These interaction parameters were calculated for $NaFeGe_2O_6$ by density functional theory [33]. Note that each Fe moment is coupled to two moments through J, to two moments through J_1, and to four moments through J_2. Since J_1 bases on two super-superexchange paths while J_2 bases only on a single path, one expects J_1 to be larger than J_2. Our inelastic neutron scattering data taken close to the $NaFeGe_2O_6$ magnetic zone origin are not sufficient to

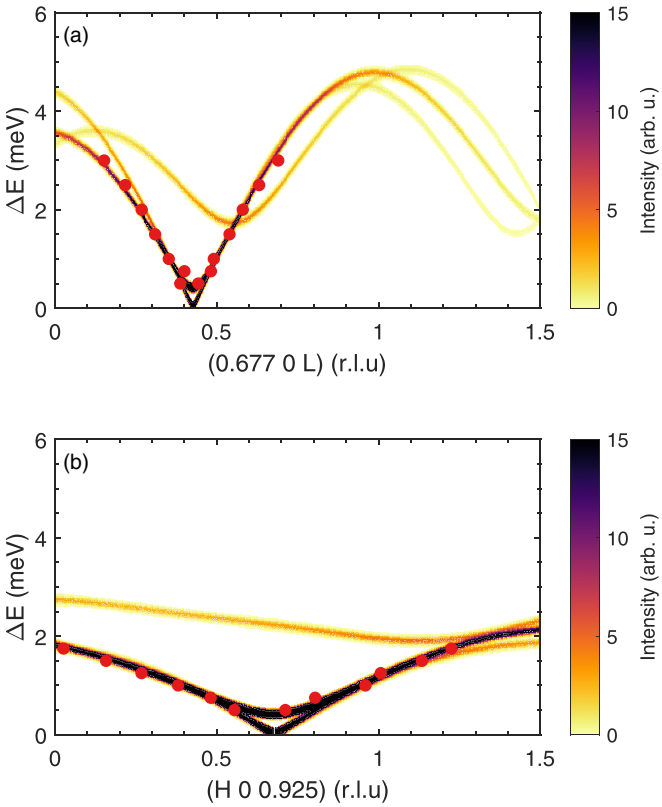

FIG. 11. Both panels show the calculated dispersion that was obatined by using *SpinW* code [60]. Hereby, the red data points correspond to the measured spin wave energies from Fig. 10.

fully solve the spin-wave dispersion of this incommensurate chiral system, for which locally transversal acoustic magnons have the character of a phason or are polarized perpendicular to the chiral plane [52,62]. Therefore, we restrict the freedom of the model. The ratio of J_1/J and J_2/J can be determined through the incommensurate propagation vector $\boldsymbol{k}_{\rm inc} = (k_h\ 0\ k_l)$ through

$$\frac{J_1}{J} = -\frac{\sin(\pi k_l)}{\sin[\pi(k_h + k_l)]}, \tag{8}$$

$$\frac{J_2}{J} = -\frac{1}{2}\frac{\sin(\pi k_l)}{\sin(\pi k_h)}. \tag{9}$$

This leaves J as the only coupling parameter to be determined; in addition, we introduce an easy-plane anisotropy term D that also stabilizes the chiral plane along the a, c plane. Figure 11 compares the calculated maps of scattering intensities with the determined spin-wave energies yielding a good description for the parameters: $J \approx 9.7$ K, $J_1 \approx 2.4$ K, and $J_2 \approx 1.3$ K and $D \approx 0.0464$ K, which qualitatively agree with the values calculated in [33]. The experimental parameters yield an antiferromagnetic Curie-Weiss temperature of 86 K in reasonable agreement with experiment. The determined J parameters reveal that the sum of interchain interaction is half as large as the intrachain interaction, which does not characterize $NaFeGe_2O_6$ as a low-dimensional system. But the interchain interaction normalized to J is even stronger for $SrMnGe_2O_6$ [61], which is thus even less low dimensional. The weakly anisotropic spin-wave dispersion seems to contrast with the magnetic susceptibility whose clear maximum at larger temperature strongly suggests a low-dimensional system. The short-range correlations are less three dimensional than the long-range order, which stems from the frustration of the two interchain interactions J_1 and J_2 [33] since these couple to the moments in the neighboring zigzag chain with and without a shift in chain direction, respectively. Since $J_2 \approx 1.3$ K coupling to twice as many sites amounts to nearly half the value of J_1, this frustration is rather perfect for a short-range correlation with strict up-down–up-down character along the chain. For the incommensurate long-range state the frustration is, however, much less effective as shown in the large spin-wave slope perpendicular to the chains. Short-range magnetic correlations and anharmonic modulation must sense a strong impact of this peculiar type of frustration.

The ferroelectric polarization is predominantly aligned along the a direction [36] and for all respective experiments on the multiferroic domain inversion, the electric field was applied parallel to a^*. In multiferroics the initial reverted regions extend along the direction of ferroelectric polarization and the subsequent sideways growth dominates the overall relaxation process [19,20]. Considering the determined spin-wave velocities, a single needle-shaped domain in the middle and the geometry of sample SII (for which the relaxation behavior was measured), the fastest possible domain relaxation is of the order of 10^{-3} ms, which agrees with the observed critical relaxation time τ^* (see Sec. V).

VII. CONCLUSION

We report investigations on the magnetic structure as well as on the multiferroic domain relaxation in $NaFeGe_2O_6$ utilizing neutron scattering experiments on single crystals. With neutron polarization analysis it is possible to separate the magnetic components of the long-range order in both phases. Thereby we can confirm the proposed incommensurate spin-density wave with moments along the a direction for the intermediate phase and a chiral spin structure with components along a and c below the multiferroic transition. In addition, there is a locking-in of the incommensurate propagation vector at $T \approx 5$ K accompanied with the emergence of a b component, whose presence was so far controversially discussed [34,35].

The multiferroic domain inversion was investigated by quasistatic as well as by time-resolved measurements of the vector chirality. Poling sequences and hysteresis loops confirm the invertibility of its sign and show low coercive fields as a function of temperature. As reported for $TbMnO_3$ [20], time-resolved measurements of the rapidly switched chiral ratio reveal the combined Arrhenius-Merz law to describe the relaxation behavior in $NaFeGe_2O_6$ over at least seven orders of magnitude in time. Even at low temperatures of the order of 1.5 K the multiferroic domain inversion is well described by thermally activated domain wall motion with only two parameters. Compared to $TbMnO_3$, $NaFeGe_2O_6$ exhibits a much shorter characteristic time corresponding to a higher domain wall velocity that is of the same order of magnitude as the spin-wave velocity. Also, the activation parameter is smaller in $NaFeGe_2O_6$ indicating weaker pinning of multiferroic

order in agreement with the small value of electric polarization in this material.

Since $NaFeGe_2O_6$ allows one to study the multiferroic domain relaxation over a large temperature range (down to $T/T_{MF} \approx 0.14$), we can analyze the scaling of electric field and reduced temperature T_r. While a simple scaling $f(\frac{T_r}{E})$ can be applied to ferroelectrics [56,57], such scaling can be excluded for the multiferroic domain relaxation in $NaFeGe_2O_6$, which follows the $f(\frac{T_r}{TE})$ scaling predicted by the Arrhenius-Merz law.

In conclusion, $NaFeGe_2O_6$ exhibits similar to $TbMnO_3$ a simple field and temperature dependence of multiferroic domain inversion that is well described by thermally activated domain wall motion with an activation field given by $A_0 \frac{T_r}{T}$.

The neutron scattering data from the IN12 diffractometer are available [63].

ACKNOWLEDGMENTS

This work was funded by the Deutsche Forschungsgemeinschaft (DFG, German Research Foundation), Project No. 277146847; CRC 1238, projects A02, B04; and by the Bundesministerium für Bildung und Forschung Project No. 05K19PK1. This work is partially based upon experiments performed at the IN12 instrument operated by JCNS at the Institute Laue-Langevin (ILL), Grenoble, France. The authors gratefully acknowledge the financial support provided by JCNS to perform the neutron scattering measurements at the Institute Laue-Langevin (ILL), Grenoble, France.

[1] N. Jones, The information factories, Nature (London) **561**, 163 (2018).
[2] J. Puebla, J. Kim, K. Kondou, and Y. Otani, Spintronic devices for energy-efficient data storage and energy harvesting, Commun. Mater **1**, 24 (2020).
[3] L. Ceze, J. Nivala, and K. Strauss, Molecular digital data storage using DNA, Nat. Rev. Genet. **20**, 456 (2019).
[4] K. N. Lin, K. Volkel, J. M. Tuck, and A. J. Keung, Dynamic and scalable DNA-based information storage, Nat. Commun. **11**, 2981 (2020).
[5] M. Wuttig and N. Yamada, Phase-change materials for rewriteable data storage, Nat. Mater. **6**, 824 (2007).
[6] R. Tomasello, E. Martinez, R. Zivieri, L. Torres, M. Carpentieri, and G. Finocchio, A strategy for the design of skyrmion racetrack memories, Sci. Rep. **4**, 6784 (2014).
[7] O. Tizno, A. R. J. Marshall, N. Fernández-Delgado, M. Herrera, S. I. Molina, and M. Hayne, Room-temperature Operation of Low-voltage, Non-volatile, Compound-semiconductor Memory Cells, Sci. Rep. **9**, 8950 (2019).
[8] A. Ghosh, G. Koster, and G. Rijnders, Multistability in bistable ferroelectric materials toward adaptive applications, Adv. Funct. Mater. **26**, 5748 (2016).
[9] M. Gu, X. Li, and Y. Cao, Optical storage arrays: a perspective for future big data storage, Light Sci. Appl. **3**, e177 (2014).
[10] J. F. Scott, Multiferroic memories, Nat. Mater. **6**, 256 (2007).
[11] N. A. Spaldin and R. Ramesh, Advances in magnetoelectric multiferroics, Nat. Mater. **18**, 203 (2019).
[12] D. Khomskii, Classifying multiferroics: Mechanisms and effects, Physics **2**, 20 (2009).
[13] M. Fiebig, T. Lottermoser, D. Meier, and M. Trassin, The evolution of multiferroics, Nat. Rev. Mater. **1**, 16046 (2016).
[14] I. E. Dzyaloshinskii, A thermodynamic theory of weak ferromagnetism of antiferromagnetics, J. Phys. Chem. Solids **4**, 241 (1958).
[15] T. Moriya, Anisotropic Superexchange Interaction and Weak Ferromagnetism, Phys. Rev. **120**, 91 (1960).
[16] M. Mostovoy, Ferroelectricity in Spiral Magnets, Phys. Rev. Lett. **96**, 067601 (2006).
[17] J. Stein, M. Baum, S. Holbein, T. Finger, T. Cronert, C. Tölzer, T. Fröhlich, S. Biesenkamp, K. Schmalzl, P. Steffens, C. H. Lee, and M. Braden, Control of Chiral Magnetism Through Electric Fields in Multiferroic Compounds Above the Long-Range Multiferroic Transition, Phys. Rev. Lett. **119**, 177201 (2017).
[18] M. Baum, J. Leist, T. Finger, K. Schmalzl, A. Hiess, L. P. Regnault, P. Becker, L. Bohatý, G. Eckold, and M. Braden, Kinetics of the multiferroic switching in $MnWO_4$, Phys. Rev. B **89**, 144406 (2014).
[19] T. Hoffmann, P. Thielen, P. Becker, L. Bohatý, and M. Fiebig, Time-resolved imaging of magnetoelectric switching in multiferroic $MnWO_4$, Phys. Rev. B **84**, 184404 (2011).
[20] J. Stein, S. Biesenkamp, T. Cronert, T. Fröhlich, J. Leist, K. Schmalzl, A. C. Komarek, and M. Braden, Combined Arrhenius-Merz Law Describing Domain Relaxation in Type-II Multiferroics, Phys. Rev. Lett. **127**, 097601 (2021).
[21] D. Niermann, C. P. Grams, M. Schalenbach, P. Becker, L. Bohatý, J. Stein, M. Braden, and J. Hemberger, Domain dynamics in the multiferroic phase of $MnWO_4$, Phys. Rev. B **89**, 134412 (2014).
[22] T. Finger, D. Senff, K. Schmalzl, W. Schmidt, L. P. Regnault, P. Becker, L. Bohatý, and M. Braden, Electric-field control of the chiral magnetism of multiferroic $MnWO_4$ as seen via polarized neutron diffraction, Phys. Rev. B **81**, 054430 (2010).
[23] S. Biesenkamp, N. Qureshi, Y. Sidis, P. Becker, L. Bohatý, and M. Braden, Structural dimerization in the commensurate magnetic phases of $NaFe(WO_4)_2$ and $MnWO_4$, Phys. Rev. B **102**, 144429 (2020).
[24] R. Kajimoto, H. Yoshizawa, H. Shintani, T. Kimura, and Y. Tokura, Magnetic structure of $TbMnO_3$ by neutron diffraction, Phys. Rev. B **70**, 012401 (2004).
[25] T. Kimura, G. Lawes, T. Goto, Y. Tokura, and A. P. Ramirez, Magnetoelectric phase diagrams of orthorhombic $RMnO_3$ (R = Gd, Tb, and Dy), Phys. Rev. B **71**, 224425 (2005).
[26] O. Prokhnenko, R. Feyerherm, M. Mostovoy, N. Aliouane, E. Dudzik, A. U. B. Wolter, A. Maljuk, and D. N. Argyriou, Coupling of Frustrated Ising Spins to the Magnetic Cycloid in Multiferroic $TbMnO_3$, Phys. Rev. Lett. **99**, 177206 (2007).
[27] S. Jodlauk, P. Becker, J. A. Mydosh, D. I. Khomskii, T. Lorenz, S. V. Streltsov, D. C. Hezel, and L. Bohatý, Pyroxenes: a new class of multiferroics, J. Phys.: Condens. Matter **19**, 432201 (2007).
[28] M. Baum, K. Schmalzl, P. Steffens, A. Hiess, L. P. Regnault, M. Meven, P. Becker, L. Bohatý, and M. Braden, Controlling

toroidal moments by crossed electric and magnetic fields, Phys. Rev. B **88**, 024414 (2013).

[29] I. Kim, B.-G. Jeon, D. Patil, S. Patil, G. Nénert, and K. H. Kim, Observation of multiferroic properties in pyroxene $NaFeGe_2O_6$, J. Phys.: Condens. Matter **24**, 306001 (2012).

[30] L. Ding, C. V. Colin, C. Darie, and P. Bordet, $SrMGe_2O_6$ (M = Mn, Co): a family of pyroxene compounds displaying multiferroicity, J. Mater. Chem. C **4**, 4236 (2016).

[31] M. Baum, A. C. Komarek, S. Holbein, M. T. Fernández-Díaz, G. André, A. Hiess, Y. Sidis, P. Steffens, P. Becker, L. Bohatý, and M. Braden, Magnetic structure and multiferroic coupling in pyroxene $NaFeSi_2O_6$, Phys. Rev. B **91**, 214415 (2015).

[32] H. Katsura, N. Nagaosa, and A. V. Balatsky, Spin Current and Magnetoelectric Effect in Noncollinear Magnets, Phys. Rev. Lett. **95**, 057205 (2005).

[33] L. Ding, P. Manuel, D. D. Khalyavin, F. Orlandi, and A. A. Tsirlin, Unraveling the complex magnetic structure of multiferroic pyroxene $NaFeGe_2O_6$: A combined experimental and theoretical study, Phys. Rev. B **98**, 094416 (2018).

[34] T. V. Drokina, G. A. Petrakovskii, L. Keller, J. Schefer, A. D. Balaev, A. V. Kartashev, and D. A. Ivanov, Modulated magnetic structure in quasi-one-dimensional clinopyroxene $NaFeGe_2O_6$, J. Exp. Theor. Phys. **112**, 121 (2011).

[35] G. J. Redhammer, A. Senyshyn, M. Meven, G. Roth, S. Prinz, A. Pachler, G. Tippelt, C. Pietzonka, W. Treutmann, M. Hoelzel, B. Pedersen, and G. Amthauer, Nuclear and incommensurate magnetic structure of $NaFeGe_2O_6$ between 5 K and 298 K and new data on multiferroic $NaFeSi_2O_6$, Phys. Chem. Miner. **38**, 139 (2011).

[36] M. Ackermann, L. Andersen, T. Lorenz, L. Bohatý, and P. Becker, Anisotropy study of multiferroicity in the pyroxene $NaFeGe_2O_6$, New J. Phys. **17**, 013045 (2015).

[37] L. Solovyova and V. Bakakin, X-ray investigation of Na, Fe-metagermanate $NaFeGe_2O_6$, Krystallographiya **12**, 591 (1967).

[38] K. Momma and F. Izumi, VESTA3 for three-dimensional visualization of crystal, volumetric and morphology data, J. Appl. Crystallogr. **44**, 1272 (2011).

[39] The measured intensity I^{expt} can be corrected for the finite flipping ratio by $I_{ii}^{\text{corr}} = I_{ii}^{\text{expt}} + 1/(\text{FR}-1)(I_{ii}^{\text{expt}} - I_{\bar{i}\bar{i}}^{\text{expt}})$ and by $I_{\bar{i}\bar{i}}^{\text{corr}} = I_{\bar{i}\bar{i}}^{\text{expt}} - 1/(\text{FR}-1)(I_{ii}^{\text{expt}} - I_{\bar{i}\bar{i}}^{\text{expt}})$, respectively.

[40] A. Poole, P. J. Brown, and A. S. Wills, Spherical neutron polarimetry (SNP) study of magneto-electric coupling in the multiferroic $MnWO_4$, J. Phys.: Conf. Ser. **145**, 012074 (2009).

[41] Y. Yamasaki, H. Sagayama, T. Goto, M. Matsuura, K. Hirota, T. Arima, and Y. Tokura, Electric Control of Spin Helicity in a Magnetic Ferroelectric, Phys. Rev. Lett. **98**, 147204 (2007).

[42] M. Janoschek, S. Klimko, R. Gähler, B. Roessli, and P. Böni, Spherical neutron polarimetry with mupad, Phys. B (Amsterdam) **397**, 125 (2007).

[43] M. Liu, L. Lin, Y. Zhang, S. Li, Q. Huang, V. O. Garlea, T. Zou, Y. Xie, Y. Wang, C. Lu, L. Yang, Z. Yan, X. Wang, S. Dong, and J.-M. Liu, Cycloidal magnetism driven ferroelectricity in double tungstate $LiFe(WO_4)_2$, Phys. Rev. B **95**, 195134 (2017).

[44] S. Biesenkamp, D. Gorkov, D. Brüning, A. Bertin, T. Fröhlich, X. Fabrèges, A. Gukasov, M. Meven, P. Becker, L. Bohatý, T. Lorenz, and M. Braden, Single-crystal investigations on the multiferroic material $LiFe(WO_4)_2$, Phys. Rev. B **103**, 134412 (2021).

[45] J. M. Perez-Mato, J. L. Ribeiro, V. Petricek, and M. I. Aroyo, Magnetic superspace groups and symmetry constraints in incommensurate magnetic phases, J. Phys.: Condens. Matter **24**, 163201 (2012).

[46] I. Urcelay-Olabarria, J. M. Perez-Mato, J. L. Ribeiro, J. L. Garcia-Munoz, E. Ressouche, V. Skumryev, and A. A. Mukhin, Incommensurate magnetic structures of multiferroic $MnWO_4$ studied within the superspace formalism, Phys. Rev. B **87**, 014419 (2013).

[47] Y. Ishibashi and Y. Takagi, Note on ferroelectric domain switching, J. Phys. Soc. Jpn. **31**, 506 (1971).

[48] Y. Ishibashi, A model of polarization reversal in ferroelectrics, J. Phys. Soc. Jpn. **59**, 4148 (1990).

[49] M. Avrami, Kinetics of phase change. i general theory, J. Chem. Phys. **7**, 1103 (1939).

[50] M. Avrami, Kinetics of phase change. ii transformationtime relations for random distribution of nuclei, J. Chem. Phys. **8**, 212 (1940).

[51] M. Avrami, Granulation, phase change, and microstructure kinetics of phase change. III, J. Chem. Phys. **9**, 177 (1941).

[52] D. Senff, P. Link, K. Hradil, A. Hiess, L. P. Regnault, Y. Sidis, N. Aliouane, D. N. Argyriou, and M. Braden, Magnetic Excitations in Multiferroic $TbMnO_3$: Evidence for a Hybridized Soft Mode, Phys. Rev. Lett. **98**, 137206 (2007).

[53] F. Kagawa, N. Minami, S. Horiuchi, and Y. Tokura, Athermal domain-wall creep near a ferroelectric quantum critical point, Nat. Commun. **7**, 10675 (2016).

[54] J. Brooke, T. F. Rosenbaum, and G. Aeppli, Tunable quantum tunnelling of magnetic domain walls, Nature (London) **413**, 610 (2001).

[55] O. G. Shpyrko, E. D. Isaacs, J. M. Logan, Y. Feng, G. Aeppli, R. Jaramillo, H. C. Kim, T. F. Rosenbaum, P. Zschack, M. Sprung, S. Narayanan, and A. R. Sandy, Direct measurement of antiferromagnetic domain fluctuations, Nature (London) **447**, 68 (2007).

[56] R. C. Miller and A. Savage, Velocity of Sidewise 180° Domain-Wall Motion in $BaTiO_3$ as a Function of the Applied Electric Field, Phys. Rev. **112**, 755 (1958).

[57] J. F. Scott, *Ferroelectric Memories, Advanced Microelectronics* (Springer, Berlin, 2000).

[58] D. Meier, N. Leo, M. Maringer, T. Lottermoser, and M. Fiebig, Topology and manipulation of multiferroic hybrid domains in $MnWO_4$, Phys. Rev. B **80**, 224420 (2009).

[59] M. Matsubara, S. Manz, M. Mochizuki, T. Kubacka, A. Iyama, N. Aliouane, T. Kimura, S. L. Johnson, D. Meier, and M. Fiebig, Magnetoelectric domain control in multiferroic $TbMnO_3$, Science **348**, 1112 (2015).

[60] S. Toth and B. Lake, Linear spin wave theory for single-q incommensurate magnetic structures, J. Phys.: Condens. Matter **27**, 166002 (2015).

[61] C. V. Colin, L. Ding, E. Ressouche, J. Robert, N. Terada, F. Gay, P. Lejay, V. Simonet, C. Darie, P. Bordet, and S. Petit, Incommensurate spin ordering and excitations in multiferroic $SrMnGe_2O_6$, Phys. Rev. B **101**, 235109 (2020).

[62] D. Senff, N. Aliouane, D. N. Argyriou, A. Hiess, L. P. Regnault, P. Link, K. Hradil, Y. Sidis, and M. Braden, Magnetic excitations in a cycloidal magnet: the magnon spectrum of multiferroic $TbMnO_3$, J. Phys.: Condens. Matter **20**, 434212 (2008).

[63] Data are available at https://doi.ill.fr/10.5291/ILL-DATA.CRG-2439 and https://doi.ill.fr/10.5291/ILL-DATA.CRG-2757.